Received: 22 May 2025 | Revised: 26 June 2025 | Accepted: 2 July 2025

DOI: 10.1002/inf2.70053

RESEARCH ARTICLE

WILEY

Unique single-phase electrocatalyst for excellent overall water splitting facilitated by multi-atom synergistic effects

Yalei Fan[1,2] | **Shengjie Zhang**[1] | **Xubin Ye**[3] | **Jing Zhou**[4] | **Qingyu Kong**[5] | **Jihao Zhang**[5] | **Youwen Long**[3] | **Jian-Qiang Wang**[1,2] | **Zhiwei Hu**[6] | **Linjuan Zhang**[1,2]

[1]Key Laboratory of Interfacial Physics and Technology, Shanghai Institute of Applied Physics, Chinese Academy of Sciences, Shanghai, the People's Republic of China

[2]University of Chinese Academy of Sciences, Beijing, the People's Republic of China

[3]Beijing National Laboratory for Condensed Matter Physics, Institute of Physics, Chinese Academy of Sciences, Beijing, the People's Republic of China

[4]Zhejiang Institute of Photoelectronics and Zhejiang Institute for Advanced Light Source, Zhejiang Normal University, Jinhua, Zhejiang, the People's Republic of China

[5]Synchrotron SOLEIL, Saint-Aubin, France

[6]Max Planck Institute for Chemical Physics of Solids, Dresden, Germany

Correspondence
Youwen Long, Beijing National Laboratory for Condensed Matter Physics, Institute of Physics, Chinese Academy of Sciences, Beijing 100190, the People's Republic of China.
Email: ywlong@iphy.ac.cn

Zhiwei Hu, Max Planck Institute for Chemical Physics of Solids, Dresden 01187, Germany.
Email: zhiwei.hu@cpfs.mpg.de

Linjuan Zhang, Key Laboratory of Interfacial Physics and Technology, Shanghai Institute of Applied Physics, Chinese Academy of Sciences, Shanghai 201800, the People's Republic of China.
Email: zhanglinjuan@sinap.ac.cn

Funding information
Strategic Priority Research Program of the Chinese Academy of Sciences, Grant/Award Number: XDA0400000; National Key R&D Program of China, Grant/Award Number: 2021YFA1400300; National Science Foundation of China, Grant/Award Numbers: 11921004,

Abstract

Hydrogen production via water electrolysis offers a sustainable pathway to decarbonize energy systems, yet the development of cost-effective, efficient bifunctional electrocatalysts for overall water splitting (OWS) still remains a critical challenge. Current catalysts often rely on complex multiphase heterostructures to optimize oxygen and hydrogen evolution reactions (OER/HER), but their intricate designs increase costs and hinder scalability. Here, we present a single-phase bifunctional electrocatalyst, $CaCu_3Co_2Ru_2O_{12}$ (CCCRO), which exhibited exceptional performance for OWS in alkaline conditions, specifically, 1.536 V at 10 mA cm^{-2} and 1.629 V at 100 mA cm^{-2}, along with 500 h of operational stability at a current density of 100 mA cm^{-2}. In situ x-ray absorption spectroscopy (XAS) revealed the valence-state transition from $Cu^{2+}/Co^{3+}/Ru^{5+}$ to $Cu^{2+}/Co^{3.5+}/Ru^{5.5+}$ during OER, but both valence state reduction and structural reconstruction into a CuCoRu nanoalloy occurred under HER conditions. Density functional theory (DFT) calculations indicated that synergistic effects among Cu, Co, and Ru ions enhance catalytic activities for both OER and HER. This work demonstrates that structurally simple yet compositionally tuned oxides can surpass complex catalysts in both

Yalei Fan, Shengjie Zhang, and Xubin Ye contributed equally to this work.

11934017, 12261131499, 12304268, 12425403, 22179141; Shanghai Municipal Science and Technology Program, Grant/Award Number: 21DZ1207700; Photon Science Center for Carbon Neutrality; Talent Plan of Shanghai Branch, the Chinese Academy of Sciences, Grant/Award Number: CASSHB-QNPD-2023-006; China Postdoctoral Science Foundation, Grant/Award Number: 2023M743741

the efficiency and durability of OWS, offering a scalable design paradigm for advancing green hydrogen technologies.

KEYWORDS

electrocatalysis, in situ XAS, overall water splitting, structure transformation, synergistic effect

1 | INTRODUCTION

The excessive extraction and utilization of non-renewable fossil fuels, such as oil, coal, and natural gas, have led to a range of severe issues, particularly environmental pollution and the greenhouse effect resulting from their combustion.[1,2] Hydrogen energy, with its distinctive advantages of zero carbon emissions, high energy density, and versatile application scenarios, is progressively transitioning from "future energy" to practical implementation.[3–5]

Green hydrogen production via water electrolysis, characterized by zero carbon emissions and efficient synergy with renewable energy sources, has emerged as a pivotal technology for achieving energy transformation and carbon neutrality. Electrocatalytic water splitting consists of two half-reactions: the hydrogen evolution reaction (HER), which produces hydrogen, and the oxygen evolution reaction (OER), which produces oxygen.[6] Although significant progress has been made in developing highly active electrocatalysts for HER and OER, there remains a critical need for efficient bifunctional catalysts to enhance the performance of overall water splitting (OWS).[7] The challenge lies in achieving simultaneous compatibility of an electrochemical catalyst with both high HER and OER activity.[8–11] Since OER and HER involve the adsorption and desorption of different intermediates (e.g., *O, *OOH, *H), both reactions suffer from sluggish kinetics and low energy efficiency,[12–14] and different electrocatalysts have traditionally been employed for the cathode and anode, such as Pt/C for HER and IrO_2 and RuO_2 for OER.[6] On the one hand, there is a pressing need to develop low-cost catalyst materials in order to reduce the cost of hydrogen production.[7,15–17] On the other hand, the distinct functional requirements of these reactions necessitate separate synthesis processes involving different materials, equipment, or procedures, as well as diverse electrode components and device fabrication methods, all of which contribute to increased system complexity and cost.[6,7,15] Moreover, under the harsh operating conditions inherent to water electrolysis—such as extreme pH levels, high potentials, and the requirement for long-term operational stability—electrocatalyst degradation (e.g., leaching and structural transformation) is inevitable. This degradation can lead to significant cross-contamination between the two electrodes, especially when composed of different materials. Therefore, utilizing the same material for both HER and OER electrocatalysts could mitigate this cross-contamination issue.[7,12,18] Consequently, there is an urgent demand for the development of highly active, durable, and economically viable bifunctional electrocatalysts capable of enabling efficient and low-cost OWS.

Currently, numerous electrocatalysts have been developed for efficient OWS.[19,20] These electrocatalysts primarily feature complex structures, such as heterojunction structures,[21–24] complex surface structures,[25–27] and so forth. Such structures not only provide a larger geometric surface area but also optimize the electronic properties of the electrocatalysts, thereby enhancing the adsorption and desorption processes of various intermediates and ultimately resulting in superior OWS performance. For example, an $Ir/SrIrO_3$ heterojunction catalyst modulated the electron distribution at the interface between Ir metal and $SrIrO_3$ perovskite, achieving an ultra-low overpotential of 229 mV for the OER and 28 mV for the HER at a current density of 10 mA cm^{-2}.[21] A V-doped $V\text{-}NiS/NiS_2$ heterojunction catalyst exhibited a dynamically balanced electronic structure during the reaction process, optimizing the adsorption and desorption of various intermediates. Consequently, the voltage of OWS was only 1.6 V at a current density of 10 mA cm^{-2}.[22] A self-assembled hierarchical $NiCo_2O_4$ hollow structure demonstrated excellent OWS performance, achieving a current density of 10 mA cm^{-2} at a voltage of merely 1.65 V.[26] However, most reported electrocatalysts for OWS have complex structures, which significantly increase design and manufacturing costs, thereby limiting their potential for large-scale applications. In contrast, relatively few single-phase catalysts have been reported as bifunctional electrocatalysts for OWS, as most single-structure catalysts cannot exhibit both HER and OER properties.[28–30] Therefore, the

development of bifunctional electrocatalysts with a single-phase structure not only simplifies the material preparation process but is also crucial for further understanding the reaction mechanisms of bifunctional electrocatalysts.

Ru element is the cheapest precious metal in the Pt group precious metal system, and it has been reported that Ru catalysts not only have excellent OER performance but also have excellent HER activity.[11,19,31–33] Therefore, Ru-based materials are expected to become highly active bifunctional OER and HER catalysts. For example, the defective-rich RuO_2 (MD-RuO_2-BN) exhibits low-coordination Ru atoms and weak Ru–O interaction, which suppresses the oxidation of lattice oxygen and the dissolution of high valence Ru, thereby demonstrating excellent OER performance (196 mV @ 10 mA cm^{-2}) and stability (1.2 mV H^{-1}).[31] The Ru–Ru_2P heterostructured catalyst, synthesized through a molten salt-assisted catalytic method, promotes charge redistribution within the catalytic system, lowers the d-band center of Ru, and thereby enhances the adsorption capacity for reaction intermediates, achieving a current density of 10 mA cm^{-2} under alkaline conditions with an overpotential as low as 18 mV.[32] The synthesized catalyst (Ru@PRC), which incorporates Ru clusters and carbon enriched with pentagonal carbon rings (PRC), optimizes the electronic structure of the catalytic system through p–d orbital hybridization between carbon and Ru, resulting in an overpotential of only 28 mV at a current density of 10 mA cm^{-2}.[33] Although numerous studies have reported Ru-based materials as highly effective catalysts for either the OER or the HER, there remains a limited number of studies focusing on their application as OWS catalysts, particularly as single-phase catalysts capable of facilitating both reactions.

Here, we report a single-phase bifunctional electrocatalyst, $CaCu_3Co_2Ru_2O_{12}$ (CCCRO), which demonstrates excellent performance for both the OER and HER in 1.0 M KOH solution. This single-phase bifunctional catalyst achieves a current density of 10 mA cm^{-2} at only 1.536 V for OWS and operates stably for 500 h at a current density of 100 mA cm^{-2} without attenuation. In situ x-ray absorption spectroscopy (XAS) indicates that CCCRO only changes its valence state without structural reconstruction during the OER process. However, during the HER, CCCRO reconstructs into a nanoalloy composed of Cu, Co, and Ru atoms. Furthermore, density functional theory (DFT) calculations reveal that Cu enhances the synergistic interactions between Cu and Co/Ru, leading to enhanced OER and HER performance.

2 | RESULTS AND DISCUSSION

2.1 | Morphology and structure

The pristine CCCRO catalyst with a quadruple perovskite structure ($AA'_3B_4O_{12}$) was synthesized via the solid-state reaction method. The crystalline phase and morphology of the pristine CCCRO were characterized using x-ray diffraction (XRD) and high-resolution transmission electron microscopy (HRTEM). The XRD pattern of the pristine CCCRO was in excellent agreement with the standard pattern of the *Im-3* space group ($CaCu_3Ru_4O_{12}$, ICSD PDF#95715), as shown in Figure S1. In this symmetry, Ca ions occupy the A site at the Wyckoff position 2*a* (0, 0, 0), Cu occupies the A′ site at 6*b* (0, 0.5, 0.5), and Co and Ru ions co-occupy the B site at 8*c* (0.25, 0.25, 0.25). Additionally, the $Ru(Co)O_6$ octahedron is connected to the CuO_4 planar quadrilateral via angle-sharing oxygen atoms (Figure S2). Rietveld refinement of the synchrotron XRD pattern was carried out to obtain the crystal structural parameters of the pristine CCCRO (Figure 1A), which were consistent with the *Im-3* space group, thereby confirming the successful synthesis of the quadruple perovskite CCCRO with Co and Ru disorder occupying the B site. Moreover, to investigate the influence of Cu ions on the performance of OWS, we also synthesized Sr_2CoRuO_6 samples. As shown in Figure S3, the XRD pattern confirmed the successful synthesis of the Sr_2CoRuO_6 in its pure phase. The pristine CCCRO was characterized using HRTEM, as illustrated in Figure 1B. The pristine CCCRO exhibited an irregular morphology with an approximate size of 38 nm (Figure 1C). The HRTEM images of the pristine CCCRO revealed distinct lattice fringes with a spacing of 0.264 nm, corresponding to the (220) crystal planes (Figure S4). Furthermore, as shown in Figure 1D, the selected area electron diffraction (SAED) pattern of the pristine CCCRO along the [111] zone axis displayed distinct diffraction spots, indicating that the pristine CCCRO possesses excellent crystallinity. Furthermore, we investigated the atomic arrangement of the pristine CCCRO nanoparticles using high-angle annular dark-field scanning transmission electron microscopy (HAADF-STEM). The HAADF-STEM image presented in Figure 1E demonstrates that the precise atomic arrangement aligns well with the theoretical perovskite structure along the (111) crystal planes. Additionally, the HAADF-STEM image indicates that the pristine CCCRO exhibits a uniform distribution of lattice fringes, with three sets of lattice fringes having interplanar spacings of 0.54 nm, which correspond to the (1 $\bar{1}$ 0), (1 0 $\bar{1}$), and (0 1 $\bar{1}$) crystal faces of the pristine CCCRO, respectively (Figure 1F). As illustrated in Figures S5 and S6, the energy-dispersive x-ray (EDX)

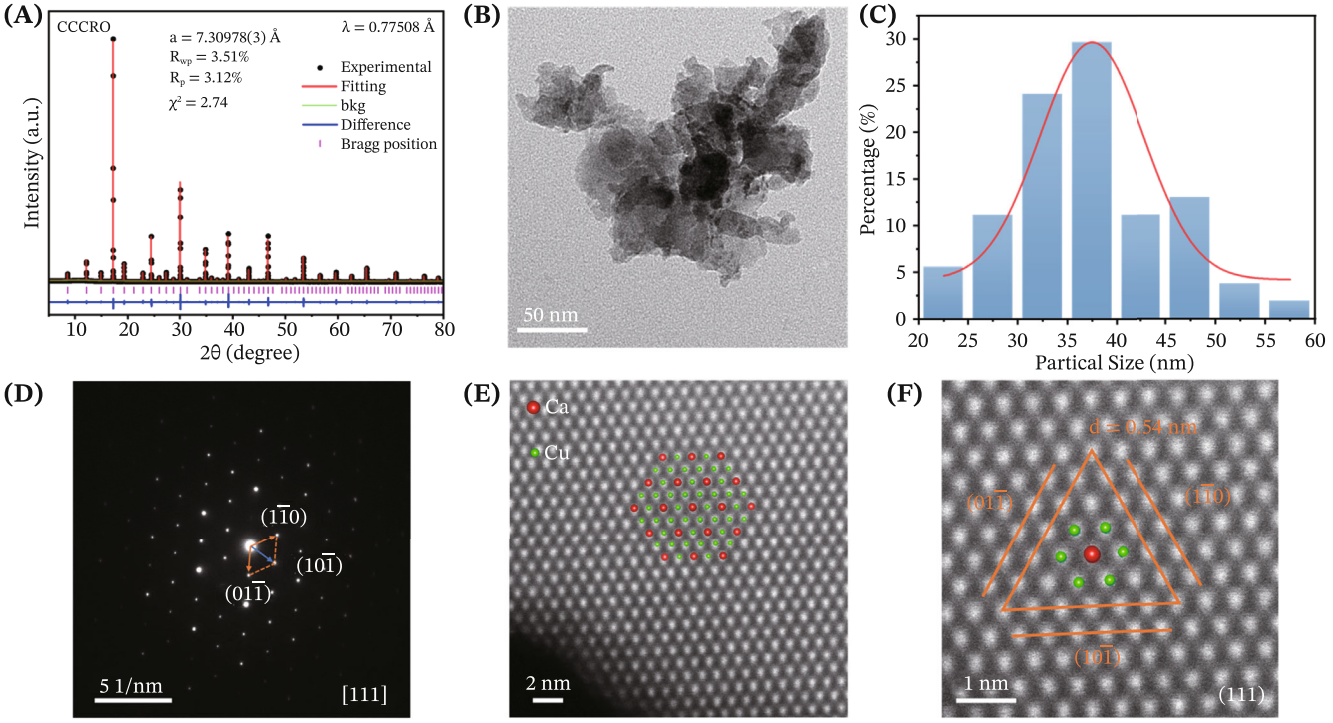

FIGURE 1 Structural and morphological characterizations of the pristine CCCRO. (A) XRD patterns. (B) HRTEM image. (C) The particle size distribution was determined using the diameters measured from the HRTEM image. (D) SAED image. (E) and (F) HAADF-STEM images.

analysis of the pristine CCCRO revealed the presence of only five elements: Ca, Cu, Co, Ru, and O. The elemental distribution was homogeneous, and their proportions adhered to the stoichiometric ratio (Table S1). Based on the above analysis, we can conclude that the CCCRO with a quadruple perovskite structure has been successfully synthesized.

2.2 | Electrocatalytic performance

To evaluate the potential of CCCRO as a bifunctional catalyst for both OER and HER, a comprehensive series of electrochemical performance tests were conducted. A conventional three-electrode system was employed to investigate the OER and HER activities of the catalyst in N_2-saturated 1.0 M KOH electrolyte. The electrocatalytic activity of CCCRO, Sr_2CoRuO_6, commercial RuO_2, and commercial 20% Pt/C for the OER and HER was assessed using linear sweep voltammetry (LSV). Notably, as shown in Figure 2A, CCCRO demonstrated superior OER performance compared to commercial RuO_2 across the entire potential range. CCCRO achieved a current density of 10 mA cm^{-2} at a potential of merely 1.428 V (vs. RHE), which is significantly lower than Sr_2CoRuO_6 (1.483 V) and commercial RuO_2 (1.529 V). Furthermore, CCCRO attained a current density of 100 mA cm^{-2} with a potential of merely 1.479 V (vs. RHE), which was 110 and 154 mV lower than those of Sr_2CoRuO_6 and commercial RuO_2, respectively (Figure 2B). This result further substantiates the superior OER activity of CCCRO and demonstrates that Cu ions can enhance the OER performance of Co–Ru based perovskites. Moreover, the Tafel slope serves as a critical parameter for assessing the reaction kinetics of the catalysts. Specifically, the Tafel slope of CCCRO was 38 mV dec^{-1}, which was considerably lower than the 80 and 83 mV dec^{-1} observed for Sr_2CoRuO_6 and commercial RuO_2, respectively, indicating that the reaction kinetics were significantly enhanced in CCCRO, as shown in Figure 2C. For the pristine CCCRO catalyst, the LSV curves after 1, 5, 10, 20, and 30 cycles of CV were obtained at a scan rate of 5 mV s^{-1}. These results indicate that the CCCRO catalyst underwent an obvious reconstruction process during the HER process (Figure S7). The reconstruction of the CCCRO catalyst can be attributed to the formation of CuCoRu alloy, which will be discussed in detail later. In Figure 2A, the commercial 20% Pt/C demonstrated superior HER performance in 1.0 M KOH at lower current densities, such as 10 and 50 mA cm^{-2}. However, as the current density increased to 100 mA cm^{-2}, CCCRO exhibited a lower voltage of −0.134 V (vs. RHE)

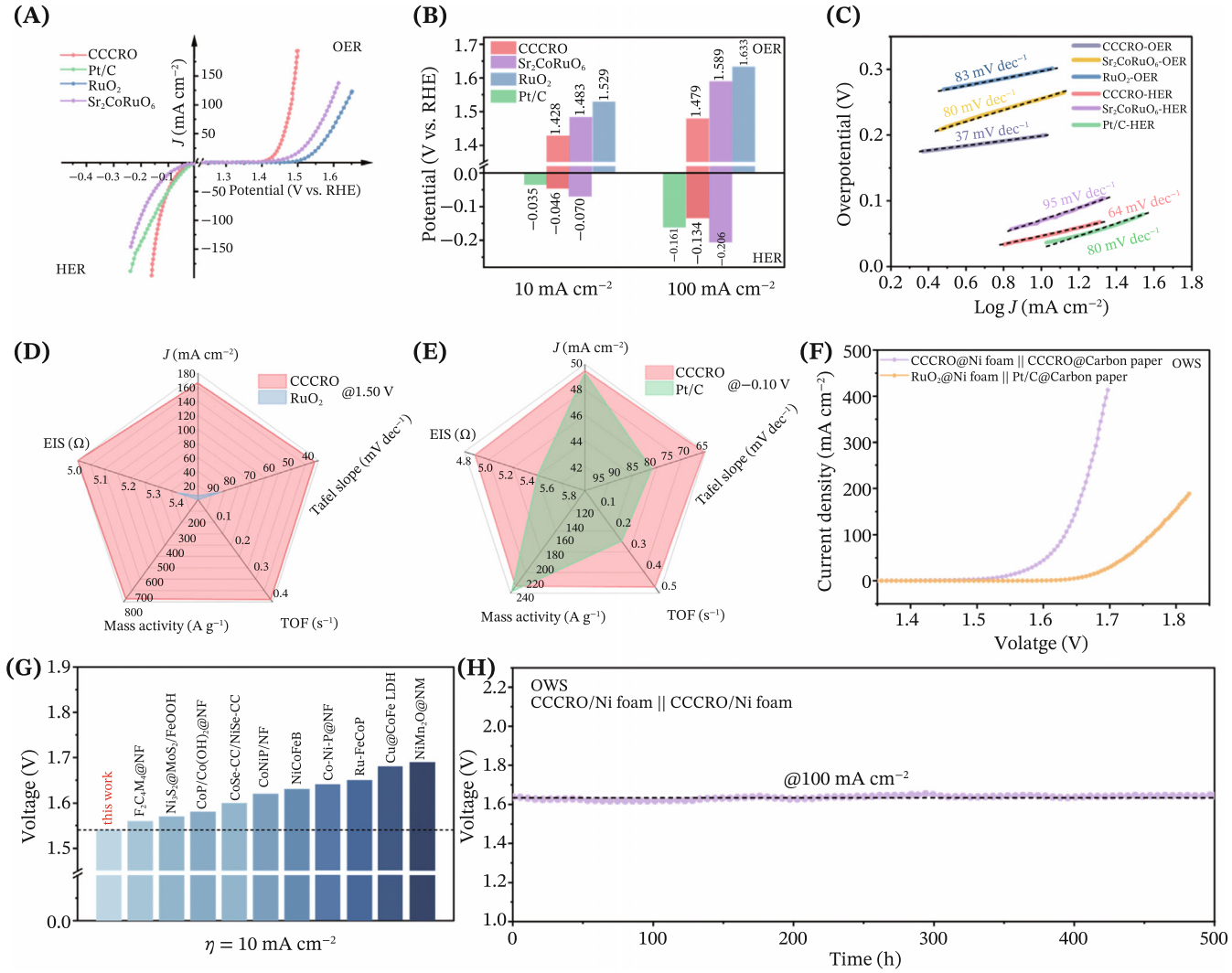

FIGURE 2 Electrocatalytic performance. (A) The LSV curves for CCCRO, Sr_2CoRuO_6, commercial RuO_2, and commercial 20% Pt/C. (B) Comparison of the overpotentials for CCCRO, Sr_2CoRuO_6, commercial RuO_2, and commercial 20% Pt/C at different current densities. (C) Tafel slopes for CCCRO, Sr_2CoRuO_6, commercial RuO_2, and commercial 20% Pt/C. Comprehensive comparisons of (D) the OER performance of CCCRO and commercial RuO_2, and (E) the HER performance of CCCRO and commercial 20% Pt/C. (F) Polarization curves in a two-electrode system. (G) Comparison of overpotentials at a current density of 10 mA cm^{-2} for CCCRO with previously reported high-activity OWS catalysts. (H) Evaluation of the long-term electrochemical stability of CCCRO for the OWS at a current density of 100 mA cm^{-2}.

compared to −0.161 V for commercial 20% Pt/C (Figure 2B). Furthermore, the catalytic performance of Sr_2CoRuO_6 was consistently lower than that of CCCRO and commercial 20% Pt/C across the entire voltage range. The Tafel slope of CCCRO was 64 mV dec^{-1}, which was significantly lower than that of commercial 20% Pt/C (80 mV dec^{-1}) and Sr_2CoRuO_6 (95 mV dec^{-1}). This also illustrates the Volmer–Heyrovsky mechanism of hydrogen evolution in the CCCRO catalyst (Figure 2C).

The electron transport rate of electrocatalysts is intrinsically linked to their conductivity. To gain deeper insights into the conductivity of the electrocatalysts, electrochemical impedance spectroscopy (EIS) was performed to assess the charge transfer resistance of the electrocatalysts (Figure S8), which confirmed that CCCRO facilitated faster charge transfer during both OER and HER. The electrochemically active surface area (ECSA) of CCCRO and the reference catalysts was determined by evaluating their electrochemical double-layer capacitance (C_{dl}) through cyclic voltammetry (CV) in the non-faradaic region at different scan rates (Figures S9 and S10). As shown in Figures S9C and S10C, the CCCRO catalyst exhibited C_{dl} values of 19.7 and 16.2 mF cm^{-2} for the OER and HER, respectively. These values were significantly higher than those of commercial RuO_2 (6.5 mF cm^{-2}) and comparable to those of commercial

20% Pt/C (17.6 mF cm^{-2}). These findings indicate that the CCCRO catalyst substantially enhances the number of active sites for both OER and HER. Furthermore, the LSV curves were also normalized by ECSA, revealing that CCCRO also exhibited higher intrinsic activity in both OER and HER (Figures S9D and S10D). The turnover frequency (TOF) of CCCRO and reference catalysts was calculated to evaluate their intrinsic electrocatalytic performance. At a potential of 1.50 V (vs. RHE), the TOF of CCCRO was 0.40 s^{-1}, which is 57 times higher than that of commercial RuO_2 (0.008 s^{-1}) (Figure S11A). At −0.15 V (vs. RHE), the TOF of CCCRO was measured at 0.71 s^{-1}, significantly exceeding the value of 0.38 s^{-1} observed for commercial 20% Pt/C (Figure S11B). Furthermore, as illustrated in Figure S12, the mass activity (MA) of CCCRO and reference catalysts was compared at different potentials. CCCRO demonstrated the highest MA values for both OER and HER. Specifically, CCCRO achieved a MA of 788.9 A g^{-1} at 1.50 V (vs. RHE), which is 38.3 times greater than that of commercial RuO_2 (Figure S12A). Additionally, at −0.15 V, the MA of CCCRO was 718.5 A g^{-1}, approximately 1.6 times higher than that of commercial 20% Pt/C (449.1 A g^{-1}) (Figure S12B).

Based on a series of comprehensive electrochemical evaluations, the performances of CCCRO in the OER and HER were systematically compared to those of commercial RuO_2 and 20% Pt/C, respectively. The results demonstrated that CCCRO exhibited superior overall performance in both OER and HER, as illustrated in Figure 2D,E. In addition to exhibiting superior OER and HER activities, excellent stability is another critical parameter for evaluating electrocatalysts. As shown in Figure S13, CCCRO was evaluated as both the cathode (loaded on carbon paper) and the anode (loaded on Ni foam) under a current density of 100 mA cm^{-2} within a conventional three-electrode system. The results demonstrated that CCCRO exhibited stable performance in 100 h with negligible attenuation, highlighting its excellent long-term stability as a catalyst for both OER and HER.

To further investigate the practical application potential of the CCCRO catalyst in alkaline conditions, a bifunctional water-splitting device was assembled using the CCCRO catalyst as both the cathode and anode. For comparison, commercial RuO_2 and 20% Pt/C were employed as the anode and cathode catalysts for the OWS, respectively. Specifically, the cathode was loaded onto carbon paper, while the anode was loaded onto Ni foam. As shown in Figures 2F and S14, at current densities of 10 and 100 mA cm^{-2}, the voltage for the CCCRO @ Ni foam||CCCRO @ Carbon paper cell was only 1.536 V and 1.629 V, respectively. This performance surpassed that of the RuO_2 @ Ni foam||20% Pt/C @ Carbon paper cell, which exhibited voltages of 1.621 V and 1.770 V at the same current densities. These results indicate that the CCCRO catalyst demonstrates superior OWS performance. Figure 2G and Table S2 present a comparison between the CCCRO catalyst and previously reported high-performance bifunctional catalysts for the OWS in alkaline conditions, demonstrating that the CCCRO bifunctional catalyst exhibits commendable OWS activity. In Figure S15, water electrolysis was conducted under a constant current of 0.1 A, with CCCRO employed as both the anode and the cathode. The hydrogen produced at the cathode and the oxygen generated at the anode were collected using the displacement method and subsequently quantified. The measured volume ratio of hydrogen to oxygen was approximately equal to the theoretical value of 2:1, suggesting that the corresponding Faraday efficiency approached 100%. As shown in Figure 2H, the CCCRO @ Ni foam||CCCRO @ Carbon paper cell was subjected to continuous testing for 500 h at a current density of 100 mA cm^{-2}, and the voltage decay rate was only 21.4 μV h^{-1}, demonstrating that the CCCRO bifunctional catalyst possesses outstanding durability and highlighting its promising prospects for industrial applications. In addition, the LSV curve after 5000 cycles of CV only showed a slight decrease compared with the initial LSV curve, indicating excellent durability during the cyclic scanning process, as shown in Figure S16. In an OWS system, the stability of OER is determined by the balance between cation leaching and the saturation of leached ions in the electrolyte. If the formation of this balance occurs before structural collapse, the catalysts remain stable; otherwise, the catalysts become unstable. For HER, anion leaching leads to the formation of metal clusters on the surface of the substrate or pure metals, whose stability plays an important role in catalytic stability. For the CCCRO bifunctional catalyst, these points are satisfied, resulting in excellent long-term operational stability.

2.3 | In situ XAS studies

Previously, it was rarely reported that materials with a single-phase structure could serve as bifunctional catalysts for OWS. In this study, we found that the CCCRO catalyst demonstrates exceptional performance in both the OER and HER. Our previous detailed study found that CCCRO experienced an increase in the oxidation states of Co and Ru ions without structural changes during the OER.[11] However, the underlying mechanisms responsible for the superior HER performance of the CCCRO catalyst and its changes during the HER remain

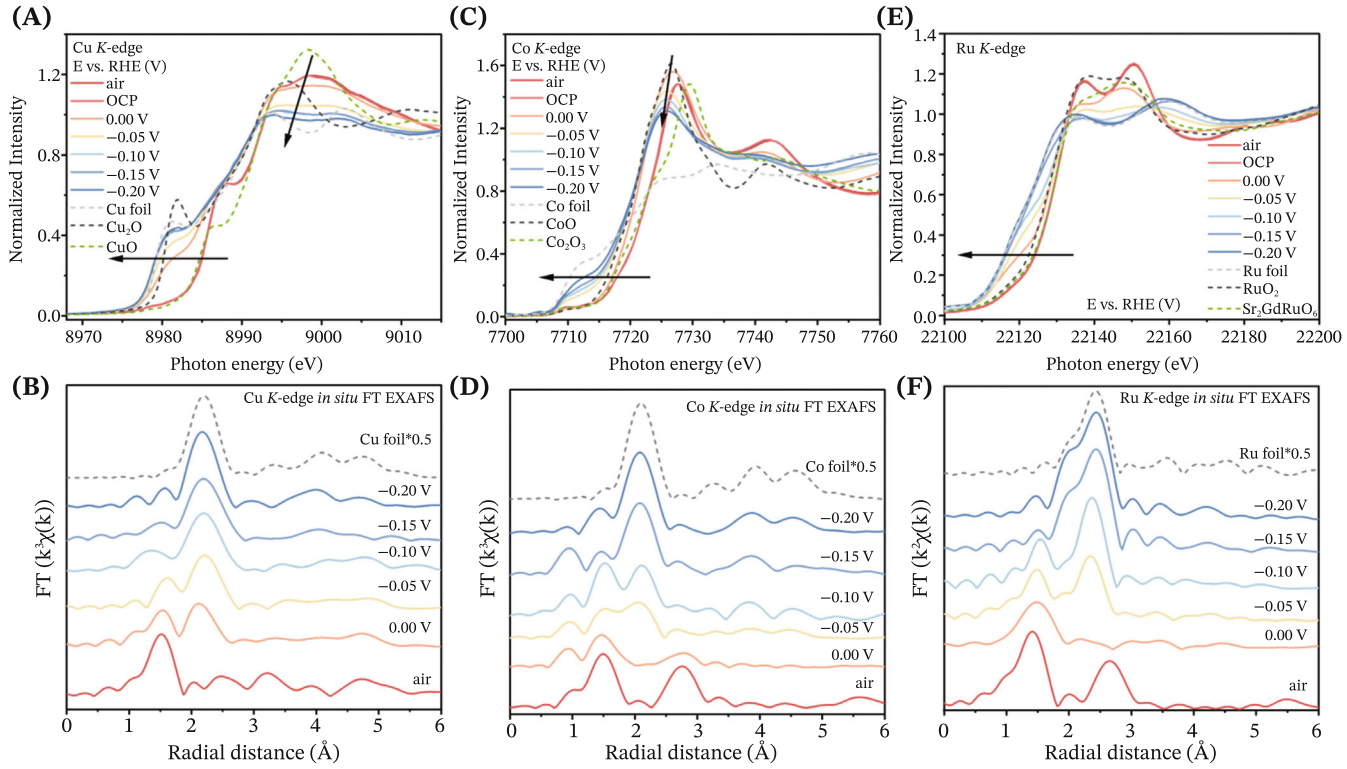

FIGURE 3 In situ XAS of CCCRO under different potentials. (A) The in situ Cu *K*-edge XANES spectra of CCCRO, along with references including Cu^0 foil, $Cu^+{}_2O$, and $Cu^{2+}O$. (C) The in situ Co *K*-edge XANES spectra of CCCRO, along with references including Co^0 foil, $Co^{2+}O$, and $Co_2{}^{3+}O_3$. (E) The in situ Ru *K*-edge XANES spectra of CCCRO, along with references including Ru^0 foil, $Ru^{4+}O_2$, and $Sr_2GdRu^{5+}O_6$. (B), (D), and (F) The in situ *K*-edge FT-EXAFS spectra of Cu, Co, and Ru in the CCCRO catalyst during the HER.

unclear. Synchrotron x-ray absorption spectroscopy (XAS) is highly sensitive to elements, oxidation states, and coordination structures.[34,35] To elucidate the relationship between the structure of the CCCRO catalyst and its catalytic activity, in situ XAS experiments were conducted.

It is well known that the *K*-edge x-ray absorption near-edge structure (XANES) of transition metals (TMs) exhibits remarkable sensitivity to their valence states,[35–37] and the extended x-ray absorption fine structure (EXAFS) demonstrates exceptional sensitivity to the local coordination environment, including coordination geometry and bond lengths.[38–41] Firstly, we analyzed the valence states and coordination structures to elucidate the electronic structure of the CCCRO in air (pristine). The XANES spectra of CCCRO in air indicated that the energy positions of the absorption edges for Cu, Co, and Ru ions were close to those of $Cu^{2+}O$, $Co_2{}^{3+}O_3$, and $Sr_2GdRu^{5+}O_6$ references (Figure 3A,C,E), respectively. The linear correlation between the energy of the absorption edge and the valence states of the standard samples further supports this conclusion (Figure S17). This correlation suggests that the oxidation states of Cu, Co, and Ru ions in the pristine CCCRO are approximately +2, +3, and +5, respectively. In addition, the Fourier Transform (FT) EXAFS results of CCCRO and the references are illustrated in Figure S18. The first radial distances of Cu–O, Co–O, and Ru–O in the pristine CCCRO are also similar to those in CuO, $LaCoO_3$, and Sr_2GdRuO_6, respectively. Figure S19 illustrates the fitting curves obtained from the FT-EXAFS of Cu, Co, and Ru ions in the pristine CCCRO. Based on the fitting results, it is evident that the Cu–O bond length is approximately 1.91 Å, forming a planar structure with four oxygen atoms (Table S3). Additionally, since the Co and Ru ions co-occupy the B-site of the perovskite structure, their fitting results are similar, including details such as coordination atom types, coordination numbers, and bond lengths (Figure S20 and Table S3).

Next, by combining in situ XAS experiments, it is possible to investigate the valence states and local environmental changes of the catalysts during the reaction process, thereby elucidating the reaction mechanism.[37,42] In Figure 3A, the Cu-*K* XANES spectra reveal that the energy position of the absorption edge for the CCCRO catalyst at the open circuit potential (OCP) closely resembles that of the $Cu^{2+}O$ reference, suggesting that the oxidation state of Cu ions at OCP remains unchanged.

During the HER, as the applied potential progressively decreases, the white line position in the Cu-*K* XANES spectra gradually shifts to lower energy, and the intensity of the white line also decreases, as shown in Figure 3A. Specifically, at an applied potential of −0.20 V (vs. RHE), the energy position of the absorption edge was found to be 1.83 eV lower than that of the air (or OCP) state. Figure 3B presents the FT-EXAFS of CCCRO as a function of applied potentials during the HER, alongside the FT-EXAFS of Cu foil for comparative analysis. As the applied potential decreases, the intensity of the Cu–O bond (∼1.51–1.61 Å) in CCCRO progressively diminishes and nearly disappears at −0.15 V (vs. RHE). In contrast, the intensity of the Cu–Cu bond (∼2.11–2.19 Å), similar to that of Cu foil, steadily increases. This observation suggests that Cu ions in CCCRO undergo reduction to metallic Cu during the HER process.

Furthermore, Figure 3C illustrates the in situ Co-*K* XANES spectra of CCCRO. In the OCP state, the energy position of the absorption edge aligns with that observed in both the air state and $Co_2^{3+}O_3$, indicating that the Co ions remained in the +3 oxidation state. During the HER process, when the applied potential was 0.0 V (vs. RHE), the energy position of the absorption edge shifted 1.82 eV to the left relative to the air state, indicating a rapid reduction in the oxidation state of Co ions from +3 to nearly +2. As the applied potential decreases further, the energy position of the absorption edge continued to shift leftward, and at an applied potential of −0.20 V (vs. RHE), the oxidation state of Co ions was evidently lower than +2. Similar to Cu ions during the HER process, this process was accompanied by a decrease in the intensity of the white line peak, and the white line shifted leftward. As illustrated in Figure 3D, when combined with the FT-EXAFS curves as a function of applied potential during the HER, it can be observed that the peaks corresponding to the Co–O bond (∼1.48–1.57 Å) and Co–Ca/Ru bonds (∼2.75 Å) attributed to CCCRO gradually diminish with the application of potential. Concurrently, when the applied potential reached −0.05 V (vs. RHE), a Co–Co bond similar to that of Co foil emerged, and the intensity of the peak increased as the applied potential decreased. This observation suggests that the metallic Co serves as an active species in the HER process.

Finally, after analyzing the changes of Cu and Co ions in the CCCRO catalyst, it is essential to confirm the changes in Ru ions during the HER and OER processes. As illustrated in Figure 3E, Ru ions in CCCRO also remained in a +5 oxidation state under the OCP condition. During the HER, in contrast to the abrupt decrease observed in Co and Cu ions, the absorption edge of the energy position of Ru ions decreased gradually. At −0.20 V (vs. RHE), the XANES spectral shape and position closely resembled those of Ru foil, indicating that Ru^{5+} in the pristine CCCRO was reduced to metallic Ru during the HER process. Further analysis of the FT-EXAFS curves of Ru ions during the HER revealed that as the applied voltage decreased, the Ru–O bond (∼1.41–1.51 Å) in the CCCRO catalyst diminished, while the peak intensity of the Ru–Ru bond (∼2.43 Å) continued to increase, as shown in Figure 3F. All findings demonstrate that the CCCRO catalyst undergoes completely different changes in the OER and HER processes. In the OER process, the CCCRO catalyst retained its perovskite structure without changes.[11] However, the active species for the HER was no longer the CCCRO perovskite but rather the CuCoRu alloy structure.

To further substantiate the in situ XAS conclusions, the CCCRO catalyst was analyzed using XRD, x-ray photoelectron spectroscopy (XPS), and HRTEM images after the HER and OER (100 mA cm^{-2} for 50 h). The XRD patterns acquired after the HER were in good agreement with the structure simulated for the $Cu_3Co_2Ru_2$ alloy, indicating that the CCCRO catalyst undergoes reconstruction into an alloy structure, as shown in Figure S21A. Moreover, the XRD pattern obtained after the OER exhibited fundamental consistency with the standard (ICSD PDF#95715), suggesting that the structure of the CCCRO catalyst remains unchanged (Figure S21B). In addition, to investigate the changes in the electronic structure of the CCCRO catalyst during the HER process, we conducted an XPS analysis. As depicted in Figure S22, after the HER, a significant proportion of Cu and Co exists in metallic states.[43,44] However, only Ru^{4+} was observed, which may be attributed to oxidation by atmospheric exposure during sample transfer. This observation underscores the critical importance of in situ XAS for identifying reactive species. As illustrated in Figure S23, the morphology of the CCCRO catalyst after the HER exhibited particles with an approximate diameter of 12 nm, indicating a significant deviation from the pristine CCCRO. Furthermore, it was clearly seen that the lattice fringes of the catalyst after the HER were consistent with those of CuCoRu alloy nanoparticles (Figure S24). Moreover, the EDX and inductively coupled plasma mass spectrometry (ICP-MS) analyses of the CCCRO catalyst after the HER indicated that Ca and O ions were nearly absent. Combined with the in situ XAS results, the continuous leaching of Ca ions and the influence of the reduction potential during the HER process led to the reduction of high-valent Cu, Co, and Ru ions to $Cu_3Co_2Ru_2$ alloy nanoparticles, as illustrated in Figures S25 and S26 and Tables S4 and S5. In Figure S27, the EDX results after the OER indicated that the elements remained evenly distributed. Furthermore, the

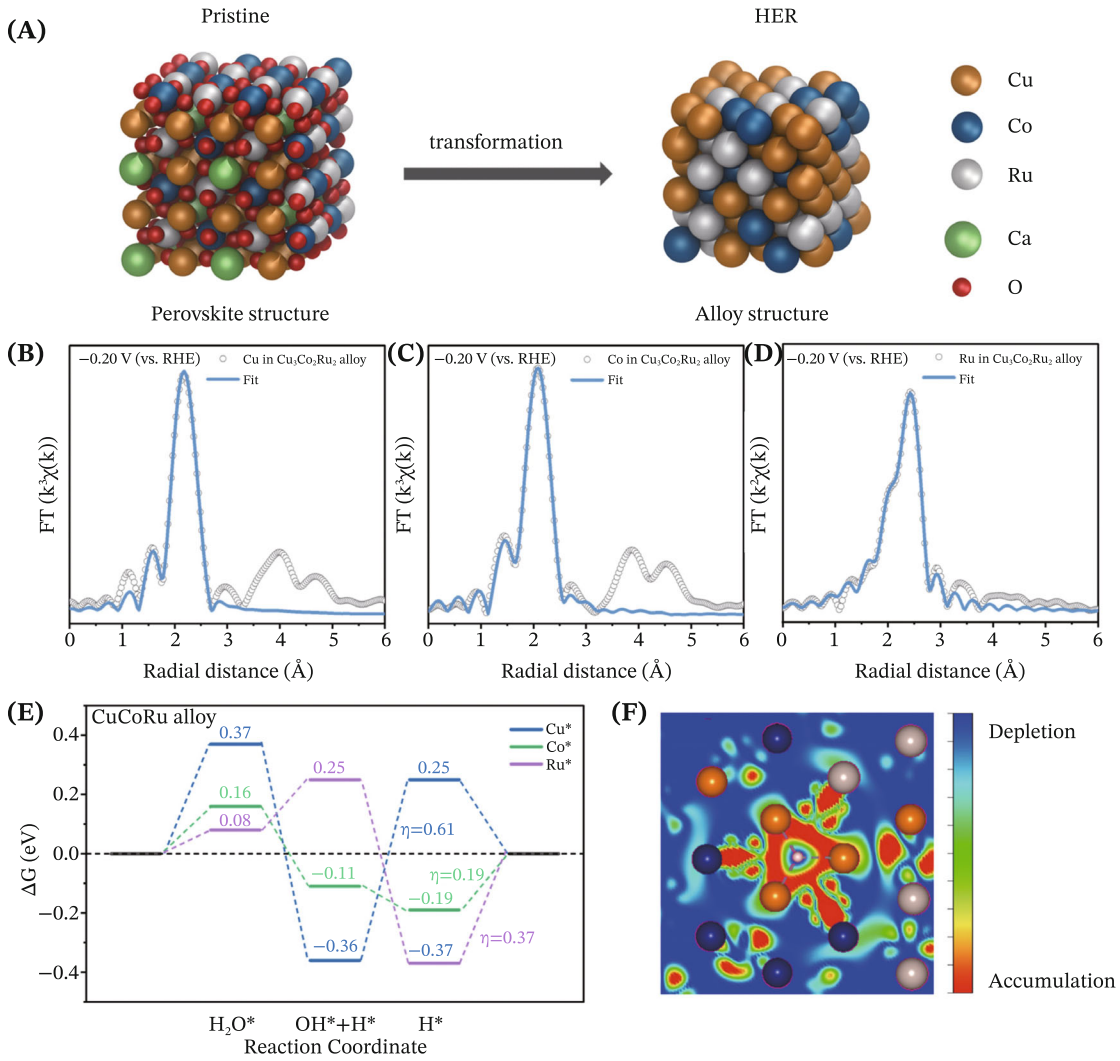

FIGURE 4 The reaction mechanism. (A) Schematic diagram illustrating the structural transformation of the CCCRO catalyst during HER process. The yellow, blue, white, green, and red balls represent Cu, Co, Ru, Ca, and O atoms, respectively. (B–D) The FT-EXAFS fitting results were obtained based on the optimized perovskite and alloy structures using DFT calculations. (E) Free energy curves for the HER. (F) The charge distribution in CuCoRu alloy structure.

after OER elemental analysis results demonstrated that partial leaching of Ca and Cu ions occurred in the CCCRO catalyst, while the atomic ratios of Co and Ru remained nearly unchanged (Tables S5 and S6). These findings not only further corroborate the in situ XAS results but also substantiate that the $Cu_3Co_2Ru_2$ alloy nanoparticles formed during the HER serve as the actual catalytic active phase.

2.4 | DFT calculation to elucidate reaction mechanisms

Previous density functional theory (DFT) calculations on the OER mechanism of CCCRO revealed that both Co and Ru sites serve as active centers participating in the lattice oxygen mechanism (LOM).[10] Additionally, the energy band structure indicated that Cu ions effectively modulate the electronic structure of CCCRO near the Fermi level, demonstrating a synergistic interaction among the Cu, Co, and Ru sites.[11]

Based on the in situ XAS and morphological analysis after the HER, it is evident that the active species transform from the perovskite into metal nanoparticles composed of Cu, Co, and Ru, as illustrated in Figure 4A. However, the underlying mechanism by which these structures enhance the reaction kinetics remains elusive. To elucidate the mechanisms responsible for the enhanced HER performance by the alloy structure, DFT was employed. Additionally, EDX (Table S4) and ICP-MS (Table S6) analyses were conducted to determine the stoichiometric ratios of elements in the alloy structure.

Firstly, to validate the accuracy of the alloy and perovskite models we constructed, we employed the theoretically optimized alloy and perovskite structures for the FT-EXAFS fitting. As illustrated in Figures 4B–D, S28, and Table S7, the structure formed at −0.2 V (vs. RHE) exhibited excellent agreement with the optimized alloy model, providing further evidence that the active phase generated during the HER was indeed the alloy structure. These results confirm the accuracy and reliability of our theoretical models.

To elucidate the active sites in the HER and establish a clear structure–activity relationship, we simulated eight distinct adsorption sites for *H intermediates on $Cu_3Co_2Ru_2$ alloy catalysts (Figure S29), calculating the corresponding Gibbs free energies (ΔG). In Figure 4E, the Cu site within the CuCoRu alloy exhibits the highest energy barrier for the rate-determining step (RDS), corresponding to the transformation process from the OH* + H* intermediate to the H* intermediate ($\Delta G = 0.61$ eV). In contrast, the RDS for both Co and Ru sites involves the transformation from H* to H_2, with respective ΔG of 0.19 eV and 0.37 eV, which are significantly lower than that of the Cu site. This indicates that both Co and Ru sites in the CuCoRu alloy serve as active sites for hydrogen evolution. Moreover, to investigate the charge transfer during the HER, the charge density difference before and after hydrogen adsorption was calculated and plotted. As illustrated in Figure 4F, the results indicate a strong interaction between the Co/Ru atoms and the neighboring Cu atoms. The analysis suggests that the Cu atoms play a crucial role in modulating the electronic structure of the Co and Ru active sites through charge transfer, thereby enhancing the HER performance of the CuCoRu alloy. This charge redistribution is a key factor in the catalytic behavior of the alloy, highlighting the importance of the Cu–Co/Ru synergy in optimizing hydrogen evolution kinetics.

3 | CONCLUSION

In summary, the single-phase CCCRO catalyst demonstrated outstanding performance in OWS, achieving a current density of 10 mA cm^{-2} at only 1.536 V, outperforming the most single-phase catalysts reported. Additionally, it exhibited high operational stability for 500 h at a current density of 100 mA cm^{-2}. In situ XAS revealed that the perovskite structure of CCCRO transformed into a CuCoRu alloy structure during the HER. The DFT calculations confirm that, although Cu is not an active site, its electronic interaction with Co/Ru reduces the energy barrier of the Co/Ru sites, thereby enhancing the HER performance. Our findings provide valuable insights into improving OWS performance through multi-element synergistic effects in a single-phase catalyst.

4 | EXPERIMENTAL SECTION

4.1 | Chemicals

The CaO (99.99%), CuO (99.99%), RuO_2 (99.995%), Co_3O_4 (99.99%), and $KClO_4$ (99.9%) were purchased from Alfa. The isopropanol (C_3H_8O, liquid, ≥99.5%) was purchased from Sinopharm Chemical Reagent Co., Ltd. The 20% Pt/C and 5 wt% Nafion solution were purchased from Aladdin. The carbon paper was purchased from Toray. The Ni foam was purchased from Sinero Technology.

4.2 | Materials synthesis

The synthesis of the CCCRO electrocatalyst was conducted using high-purity CaO, CuO, Co_3O_4, RuO_2, and $KClO_4$ powders as starting materials via a solid-state reaction under high-pressure and high-temperature conditions. In this process, $KClO_4$ served as an oxygen source to minimize oxygen vacancies in the synthesized quadruple perovskite sample. The blended mixture was encapsulated in a platinum capsule, which was heated by a graphite heater and electrically insulated with hexagonal BN sleeves. Molybdenum plates were used as the conductive electrodes, and cubic pyrophyllite blocks served as the pressure medium. The entire high-pressure assembly was loaded into a DIA-type cubic six-anvil apparatus, where it was subjected to a pressure of 8 GPa. The sample was then heated at a rate of 100 K min^{-1} to 1550 K, held for 30 min, and subsequently quenched rapidly with an estimated cooling rate of ∼1000 K min^{-1}. The resultant powder sample was thoroughly washed with deionized water to remove any residual KCl, and then ball-milled to obtain a high-quality electrocatalyst for subsequent characterization and measurement.

4.3 | Structural characterization

The structure of the electrocatalysts was characterized using x-ray diffraction (XRD) with a Bruker D8 Advance diffractometer. Synchrotron XRD was performed using a large Debye–Scherrer camera installed at the BL02B2 beamline ($\lambda = 0.77508$ Å) of SPring-8. The morphology of electrocatalysts was examined through high-resolution transmission electron microscopy (HRTEM) utilizing an FEI Tecnai G2 F20 microscope operating at 200 kV. In

addition, high-angle annular dark-field scanning transmission electron microscopy (HAADF-STEM) images were captured with an aberration-corrected FEI Themis Z STEM microscope. The Cu and Co *K*-edge x-ray absorption spectra (XAS) were collected at an in-house laboratory-based x-ray absorption spectrometer (SuperXAFS M9000) and at the Shanghai Synchrotron Radiation Facility (SSRF) on the BL20U beamline. For the Ru *K*-edge XAS spectra, measurements were conducted at the SSRF on the 14 W1 beamline and at the Synchrotron SOLEIL on the ODE beamline. All *K*-edge XAS data were processed and analyzed using the Demeter software.[45] The energy calibration was performed based on the absorption edges of Cu, Co, and Ru foils.

4.4 | Electrochemical measurements

The electrochemical performance of the catalysts for the oxygen evolution reaction (OER) and the hydrogen evolution reaction (HER) was conducted in a 1.0 M KOH solution, using an electrochemical workstation (Metrohm Autolab with a PGSTAT 302 N system). A glassy carbon electrode (GCE) served as the working electrode, while a carbon rod acted as the counter electrode, and a Hg/HgO electrode (with 1.0 M KOH solution) was used as the reference electrode. Initially, 5 mg of the catalyst powder and 5 mg of carbon black were mixed into a solution comprising 700 μL of deionized water and 250 μL of isopropanol. Subsequently, 40 μL of Nafion solution was added to the mixture, which was then sonicated in an ultrasonic bath for 1 h. Following this, 8 μL of the prepared catalyst ink was carefully deposited onto a polished glassy carbon electrode (GCE) with a diameter of 5 mm (0.196 cm^2, loading of 0.2 mg cm^{-2}), which served as the working electrode. The potential conversion from the Hg/HgO to the reversible hydrogen electrode (RHE) scale was calculated using the equation $E(\text{RHE}) = E(\text{Hg/HgO}) + 0.059*\text{pH} + 0.0977$ V. For the impedance spectroscopy measurements, the frequency range employed was from 10^5 to 10^{-2} Hz. The measured potentials were referenced to the RHE, and the potential losses due to electrolyte resistance were corrected using a 90% iR-drop compensation. The performance of alkaline overall water splitting was assessed in a two-electrode setup using a 1.0 M KOH solution. The CCCRO catalyst was loaded onto carbon paper and Ni foam with an area of 1 cm^2 (1 cm × 1 cm) as the cathode and anode, respectively, with a loading of 0.5 mg cm^{-2}.

4.5 | Theory calculations

The calculations were conducted using density functional theory (DFT) with the Perdew, Burke, and Ernzerhof generalized gradient functional (GGA-PBE) using the Vienna Ab initio Simulation Package (VASP).[46–48] A 4 × 4 × 1 k-point mesh was employed, with a cutoff energy of 400 eV. The force and energy convergence criteria were set to 0.03 eV $Å^{-1}$ and 10^{-5} eV, respectively. The top two layers and the adsorbates were allowed to fully relax during relaxation calculations. A vacuum gap of approximately 15 Å was set along the surface normal direction.

ACKNOWLEDGMENTS

This work was supported by the Strategic Priority Research Program of the Chinese Academy of Sciences (No. XDA0400000), the National Key R&D Program of China (Grant No. 2021YFA1400300), the National Science Foundation of China (Grant No. 22179141, 12425403, 12304268, 12261131499, 11934017, and 11921004), the Shanghai Municipal Science and Technology Program (Grant No. 21DZ1207700), the Photon Science Center for Carbon Neutrality, the Talent Plan of Shanghai Branch, the Chinese Academy of Sciences (CASSHB-QNPD-2023-006), and the China Postdoctoral Science Foundation (Grant No. 2023M743741). The powder synchrotron x-ray diffraction experiments were performed at SPring-8 with the approval of the Japan Synchrotron Radiation Research Institute (2024A1506). The authors acknowledge support from the Max Planck-POSTECH-Hsinchu Center for Complex Phase Materials. Open Access funding enabled and organized by Projekt DEAL.

CONFLICT OF INTEREST STATEMENT

The authors declare no conflict of interest.

DATA AVAILABILITY STATEMENT

The data that support the findings of this study are available from the corresponding author upon reasonable request.

ORCID

Linjuan Zhang https://orcid.org/0000-0003-4704-5807

REFERENCES

1. Xie H, Zhao Z, Liu T, et al. A membrane-based seawater electrolyser for hydrogen generation. *Nature*. 2022;612(7941):673-678.
2. Liu W, Ding X, Cheng J, et al. Inhibiting dissolution of active sites in 80°C alkaline water electrolysis by oxyanion engineering. *Angew Chem Int ed*. 2024;63(32):e202406082.
3. Service RF. New electrolyzer splits water on the cheap. *Science*. 2020;367(6483):1181.
4. Long Z, Yu C, Cao M, Ma J, Jiang L. Bioinspired gas manipulation for regulating multiphase interactions in electrochemistry. *Adv Mater*. 2024;36(21):2312179.
5. Liu G, Wong WS, Kraft M, et al. Wetting-regulated gas-involving (photo)electrocatalysis: biomimetics in energy conversion. *Chem Soc Rev*. 2021;50(18):10674-10699.

6. Wang X, She G, Mu L, Shi W. Amorphous Co–Mo–P–O bifunctional electrocatalyst via facile electrodeposition for overall water splitting. *ACS Sustainable Chem Eng*. 2020;8(7):2835-2842.
7. Quan L, Jiang H, Mei G, Sun Y, You B. Bifunctional electrocatalysts for overall and hybrid water splitting. *Chem Rev*. 2024;124(7):3694-3812.
8. Zang W, Sun T, Yang T, et al. Efficient hydrogen evolution of oxidized Ni–N_3 defective sites for alkaline freshwater and seawater electrolysis. *Adv Mater*. 2021;33(8):2003846.
9. Park YS, Lee J, Jang MJ, et al. High-performance anion exchange membrane alkaline seawater electrolysis. *J Mater Chem A*. 2021;9(15):9586-9592.
10. Cai C, Liu K, Zhu Y, et al. Optimizing hydrogen binding on Ru sites with RuCo alloy nanosheets for efficient alkaline hydrogen evolution. *Angew Chem Int ed*. 2022;134(4):e202113664.
11. Fan Y, Ye X, Zhou J, et al. Combined in situ X-ray spectroscopic and theoretical study on trimetal synergistic enhancement of water oxidation. *Adv Energy Mater*. 2025;15(15):2404599.
12. Sun H, Yan Z, Tian C, et al. Bixbyite-type Ln_2O_3 as promoters of metallic Ni for alkaline electrocatalytic hydrogen evolution. *Nat Commun*. 2022;13(1):3857.
13. Li Y, Zhang J, Chen Q, Xia X, Chen M. Emerging of heterostructure materials in energy storage: a review. *Adv Mater*. 2021;33(27):2100855.
14. Chen D, Lu R, Yu R, et al. Work-function-induced interfacial built-in electric fields in Os–$OsSe_2$ heterostructures for active acidic and alkaline hydrogen evolution. *Angew Chem Int Ed*. 2022;61(36):e202208642.
15. Meskher H, Woldu AR, Chu PK, Lu F, Hu L. Sustainability assessment of seawater splitting: prospects, challenges, and future directions. *EcoEnergy*. 2024;2(4):630-651.
16. Jang JU, Gaur A, Mhin S, Han H. Fabrication of self-supported catalysts via electrodeposition for proton exchange membrane water electrolysis: emphasizing on the porous transport layers. *EcoEnergy*. 2024;2(3):381-399.
17. Han C, Jiang J, Mu L, et al. Quasi-vertically asymmetric channels of graphene oxide membrane for ultrafast ion sieving. *Nat Commun*. 2025;16(1):1020.
18. Du Y, Li B, Xu G, Wang L. Recent advances in interface engineering strategy for highly-efficient electrocatalytic water splitting. *InfoMat*. 2023;5(1):e12377.
19. Liu J, Ren J, Du Y, et al. V-doping strategy induces the construction of the functionally complementary Ru_2P/V-RuP_4 heterostructures to achieve amperometric current density for HER. *Adv Funct Mater*. 2024;34(28):2315773.
20. Hu F, Yu D, Ye M, et al. Lattice-matching formed mesoporous transition metal oxide heterostructures advance water splitting by active Fe–O–Cu bridges. *Adv Energy Mater*. 2022;12(19):2200067.
21. Zhang B, Wu Z, Shao W, et al. Interfacial atom-substitution engineered transition-metal hydroxide nanofibers with high-valence Fe for efficient electrochemical water oxidation. *Angew Chem Int Ed*. 2022;134(13):e202115331.
22. Zhao L, Tao Z, You M, et al. Partial exsolution enables superior bifunctionality of Ir@$SrIrO_3$ for acidic overall water splitting. *Adv Sci*. 2024;1(24):2309750.
23. Xu W, Zhao R, Li Q, et al. Overall water splitting on the NiS/-NiS_2 heterostructures featuring self-equilibrium orbital occupancy. *Adv Energy Mater*. 2023;13(31):2300978.
24. Yaseen W, Xie M, Yusuf BA, et al. Anchoring $Ni(OH)_2$–CeO_x heterostructure on FeOOH-modified nickel-mesh for efficient alkaline water-splitting performance with improved stability under quasi-industrial conditions. *Small*. 2024;20(44):2403971.
25. Jiang H, Zhao Z, Li G, et al. Hollow spherical heterostructured FeCo-P catalysts derived from MOF-74 for efficient overall water splitting. *Adv Sci*. 2024;11(2):2306919.
26. Gao X, Zhang H, Li Q, et al. Hierarchical $NiCo_2O_4$ hollow microcuboids as bifunctional electrocatalysts for overall water-splitting. *Angew Chem Int Ed*. 2016;55(21):6290.
27. Moloudi M, Noori A, Rahmanifar MS, et al. Layered double hydroxide templated synthesis of amorphous NiCoFeB as a multifunctional electrocatalyst for overall water splitting and rechargeable zinc-air batteries. *Adv Energy Mater*. 2023;13(4):2203002.
28. Thiyagarajan D, Thirumurugan A, Lee B-K. Construction of NiS@$CoFeMoO_4$/NF nanosheet heterostructures for efficient overall water splitting. *Int J Hydrogen Energy*. 2022;47:39908.
29. Sarmad Q, Khan UM, Baig MM, et al. Praseodymium-doped Sr_2TiFeO_{6-d} double perovskite as a bi-functional electrocatalyst for hydrogen production through water splitting. *J Environ Chem Eng*. 2022;10(3):107609.
30. Zhang W, Xue M, Zhang X, et al. Boosting oxygen/hydrogen evolution catalysis via ruthenium doping in perovskite oxide for efficient alkaline water splitting. *Appl Surf Sci*. 2022;664:160278.
31. Chen D, Yu R, Yu K, et al. Bicontinuous RuO_2 nanoreactors for acidic water oxidation. *Nat Commun*. 2024;15(1):3928.
32. Chen D, Yu R, Lu R, et al. Tunable Ru–Ru_2P heterostructures with charge redistribution for efficient pH-universal hydrogen evolution. *InfoMat*. 2022;4(5):e12287.
33. Gong L, Xia F, Zhu J, et al. Hydrogen evolution reactivity of pentagonal carbon rings and p–d orbital hybridization effect with Ru. *Angew Chem Int ed*. 2024;63(50):e202411125.
34. Zhu Y, Zhou W, Zhong Y, et al. A perovskite nanorod as bifunctional electrocatalyst for overall water splitting. *Adv Energy Mater*. 2027;7(8):1602122.
35. Li L, Sun H, Hu Z, et al. In situ/operando capturing unusual Ir^{6+} facilitating ultrafast electrocatalytic water oxidation. *Adv Funct Mater*. 2021;31(43):2104746.
36. Huang H, Chang Y-C, Huang Y-C, et al. Unusual double ligand holes as catalytic active sites in $LiNiO_2$. *Nat Commun*. 2023;14(1):2112.
37. Fan Y, Zhang C, Zhang L, et al. Novel mechanism of Fe^{4+}/Ni^{3+} synergistic effect via exchange energy gain for boosting water oxidation. *Chem Catal*. 2024;4(5):100981.
38. Zhou J, Hu Y, Chang Y-C, et al. In situ exploring of the origin of the enhanced oxygen evolution reaction efficiency of metal(Co/Fe)-organic framework catalysts via postprocessing. *ACS Catal*. 2022;12(5):3138-3148.
39. Lin X, Huang Y-C, Hu Z, et al. 5f covalency synergistically boosting oxygen evolution of $UCoO_4$ catalyst. *J Am Chem Soc*. 2021;144(1):416-423.
40. Zhang L-J, Wang J-Q, Li J, et al. High-Tc ferromagnetism in a Co-doped ZnO system dominated by the formation of a zinc-

blende type Co-rich ZnCoO phase. *Chem Commun*. 2012;48(1): 91-93.
41. Jing C, Li L, Chin Y-Y, et al. Balance between Fe^{IV}–Ni^{IV} synergy and lattice oxygen contribution for accelerating water oxidation. *ACS Nano*. 2024;18(22):14496-14506.
42. Hu Y, Fan Y, Li L, et al. Modulating 3D charge state via halogen ions in neighboring molecules of metal-organic frameworks for improving water oxidation. *Small*. 2024;20(34): 2400042.
43. Li Y, Zhang H, Li D, Xie J, Chang A. Influence of cationic vacancy diffusion on the aging behavior of low-temperature $SrCo_{1-x}Ru_xO_3$ thermosensitive ceramics. *Ceram Int*. 2024; 50(15):27496-27507.
44. Wang W, Yang Y, Huan D, et al. An excellent OER electrocatalyst of cubic $SrCoO_{3-\delta}$ prepared by a simple F-doping strategy. *J Mater Chem A*. 2019;7(20):12538.
45. Ravel B, Newville M. ATHENA, ARTEMIS, HEPHAESTUS: data analysis for x-ray absorption spectroscopy using IFEFFIT. *J Synchrotron Radiat*. 2005;12(4):537-541.
46. Kresse G, Furthmüller J. Efficient iterative schemes for ab initio total-energy calculations using a plane-wave basis set. *Phys Rev B*. 1996;54(16):11169-11186.
47. Kresse G, Joubert D. From ultrasoft pseudopotentials to the projector augmented-wave method. *Phys Rev B*. 1999;59(3): 1758-1775.
48. Perdew JP, Burke K, Ernzerhof M. Generalized gradient approximation made simple. *Phys Rev Lett*. 1996;77(18):3865-3868.

SUPPORTING INFORMATION

Additional supporting information can be found online in the Supporting Information section at the end of this article.

How to cite this article: Fan Y, Zhang S, Ye X, et al. Unique single-phase electrocatalyst for excellent overall water splitting facilitated by multi-atom synergistic effects. *InfoMat*. 2025;7(10): e70053. doi:10.1002/inf2.70053